Electrochimica Acta 530 (2025) 146413

Contents lists available at ScienceDirect

Electrochimica Acta

journal homepage: www.journals.elsevier.com/electrochimica-acta

Multilayer MXene framework for construction of hierarchical structure composites for high performance metal ion batteries

Peng Guo [a,b,*], Lennart Singer [a], Zhiyong Zhao [c], Brian Hinz [a], Tomasz Kędzierski [d], Tobias König [a], Ewa Mijowska [d], Michael Zharnikov [c], Peter Comba [b,*], Rüdiger Klingeler [a,*]

[a] Kirchhoff Institute for Physics, Heidelberg University, Im Neuenheimer Feld 227, D-69120, Heidelberg, Germany
[b] Anorganisch-Chemisches Institut, Universität Heidelberg, Im Neuenheimer Feld 270, D-69120, Heidelberg, Germany
[c] Angewandte Physikalische Chemie, Universität Heidelberg, Im Neuenheimer Feld 253, D-69120, Heidelberg Germany
[d] Department of Nanomaterials Physicochemistry, Faculty of Chemical Technology and Engineering, West Pomeranian University of Technology, Piastów Av. 45, Szczecin, 70-311, Poland

ARTICLE INFO

Keywords:
MXene
Hierarchical structure
Composite
Lithium ion battery
Molybdenum dioxide

ABSTRACT

MXenes have become promising candidates for metal ion battery anodes. However, the achievable capacities of bare MXene-based electrodes are still limited. A promising strategy to overcome this issue and still exploit the unique properties of MXenes is to design composites of the MXenes and high-capacity conversion or alloy-type anode materials. Despite the growing interest in these kinds of MXene-based composites, the utility of multilayer MXene with its unique accordion-like structure is, even though it promises many advantages, such as a large surface area and a unique open structure, rarely reported. Here, we report on the preparation of hierarchical $MoO_2/C/V_2C$ composites by an electrostatic interaction-assisted hydrothermal method and a post-annealing process. Our composites exhibit a unique hierarchical structure, where the MoO_2 nanoparticles are confined and uniformly distributed in the open V_2C/C layered framework. This architecture enables fast-ion and electron transfers and nicely accommodates the volume changes of MoO_2 during cycling. Therefore, when used for lithium-ion batteries, the composites exhibit outstanding long-term cycling performance at high current densities of 1 and 2 A g^{-1}. Our results demonstrate the benefits of using an accordion-like MXene host-framework for the composite formation and highlight the potential of such composites for high performance metal ion batteries.

1. Introduction

MXenes, a new class of two-dimensional materials, which was first reported by Gogotsi's group[1], have attracted widespread interest in multiple fields such as energy storage, energy conversion and electromagnetic interference shielding[2–5]. Particularly, high conductivity, excellent mechanical stability and variable surface chemistry make MXenes promising potential anode materials for metal ion batteries [6–10]. However, even though the capacity attained for recently reported MXene-based electrodes appears to be highly reversible, it is still limited. For instance, Ti_3C_2, Nb_2C, and V_2C exhibit reversible capacities of less than 400 mAh g^{-1} for lithium ion batteries (LIBs) and 300 mAh g^{-1} for sodium ion batteries (SIBs) [11–13]. Other known high-capacity anodes like conversion and alloy-type materials on the contrary display insufficient cycling stability as they suffer from severe phase transformation and volume expansion during the cycling process, resulting in the pulverization of active materials and thereafter rapid capacity degradation. A promising strategy to simultaneously exploit the unique properties of MXenes and achieve high electrochemical capacity is to design composites of MXenes and high-capacity conversion or alloy-type anode materials, such as metal oxides, metal sulfides and silicon[14–18].

In order to fabricate such composite materials, exfoliated MXene nanosheets are generally adopted to form composites by in-situ growth or liquid assembly methods. In particular, within this strategy, Bashir et al. prepared an MXene-supported $Si@V_2C$ composite by a sonication-assisted method[19]. When used as anode material in lithium-ion battery, this $Si@V_2C$ composite displayed a reversible capacity of 430 mAh g^{-1} after 150 cycles at 200 mA g^{-1}. Another representative example is the study of Ai et al. synthesizing SnS nanoparticles anchored in Ti_3C_2 nanosheet matrix composites via an electrostatic attraction method[20]. The resulting composite electrode showed a specific capacity of 646

* Corresponding authors.
E-mail addresses: pengguokip25@163.com (P. Guo), peter.comba@aci.uni-heidelberg.de (P. Comba), klingeler@kip.uni-heidelberg.de (R. Klingeler).

https://doi.org/10.1016/j.electacta.2025.146413
Received 30 March 2025; Received in revised form 2 May 2025; Accepted 6 May 2025
Available online 7 May 2025

mAh g^{-1} at the current density of 100 mAg^{-1} after 100 cycles. A few further examples can be found in the recent review by Bi et al. [21]

On the contrary, unexfoliated multilayer MXene with the unique accordion-like structure has, despite many promising advantages, rarely been reported as a host structure for composite formation. The main advantage of unexfoliated multilayer MXenes is their unique 'open structure', which arises due to the applied synthesis conditions[1]. Such attainable MXene structures ensure good contact between electrolyte and electrode, which is beneficial for fast electron and ion transfer. Also, in our opinion, the unexfoliated multilayer MXene structure is a suitable framework for the further composite formation with conversion and alloy-type anode materials, as the robust open structure promises to mitigate the strong volume expansion that occurs with pure conversion-type and alloy-type anode materials by their confinement into the hierarchical structure. A promising high-capacity candidate to be introduced into such a hierarchical structure is the conversion-type material molybdenum dioxide (MoO_2) owing to its high theoretical capacity (838 mAh/g), lower-cost molybdenum precursors compared to metal chalcogenides (e.g., Re_2Te_5, $CoTe_2$, Bi_2Te_3, $ReSe_2$, SnS_2), and environmentally benign preparation via facile hydrothermal-annealing method[22–26]. Regardless of the unique benefits and promises of such composites, a big challenge that is not easily overcome was and is the uniform integration of MXenes with other materials present, due to the poor dispersibility of multilayer MXene in the solvent.

Here, we report the preparation of hierarchical $MoO_2/C/V_2C$ composites by an electrostatic interaction-assisted hydrothermal method and a post-annealing process. We solved the problem of low dispersibility of V_2C-MXene and simultaneously modified the surface charge state of V_2C-MXene for the optimized combination with MoO_2 through the usage of the cationic polydiallyldimethylammonium chloride (PDDA). The resultant $MoO_2/C/V_2C$ composites exhibit a hierarchical structure, where MoO_2 nanoparticles are confined in the open V_2C/C layered structure. Thanks to this unique structure, when used for the lithium ion battery, the $MoO_2/C/V_2C$ composites exhibit excellent electrochemical performance featuring superior rate capability and long-term cycling stability. In particular, the here presented $MoO_2/C/V_2C$ composites with molybdenum-source $(NH_4)_6Mo_7O_{24}$:V_2C precursor mass ratios of 4:1 and 8:1 deliver high specific capacities of 603 and 420 mAh g^{-1}, respectively, after 400 cycles at a current density of 1000 mA g^{-1}. These results confirm the great potential of multilayer MXenes as a host framework and demonstrate the applicability of this type of structure for composite formation with other anode materials.

2. Experimental section

2.1. *Synthesis of $MoO_2/C/V_2C$ composites*

V_2C: V_2C-MXene was synthesized by etching the aluminum layer out of the precursor (V_2AlC: Jilin 11 Technology Co., Ltd) with the help of a mixed solution of LiF and HCl. The etching solution was prepared by dissolving 1 g LiF powder in a 9 M HCl solution followed by a magnetically stirring time of 2 h. The etching solution can in-situ form HF solution which exposure is very toxic and should be prepared in an HF lab. The precursor V_2AlC was then immersed into the above solution and the mixture was transferred to a 50 ml stainless steel autoclave lined with PTFE and heated at 90 °C for 72 h. The precipitate (V_2C-MXene) was collected after centrifugation, washed several times with water and ethanol until the pH value of the solution was above 5, and dried in an oven at 60 °C for 24 h.

V_2C/PDDA: The positively charged V_2C/PDDA was prepared by modifying V_2C with PDDA (Aldrich, 20 wt% in water) solution. In detail, 50 mg V_2C was firstly dispersed in 30 mL water. Afterwards, 1 ml PDDA solution (20 wt%) was added dropwise to the above V_2C solution under continuous stirring for 2 h.

$MoO_2/C/V_2C$: The $MoO_2/C/V_2C$ composites were prepared via a hydrothermal and annealing process. 400 or 200 mg of $(NH_4)_6Mo_7O_{24}$ was added to a V_2C/PDDA solution under vigorous stirring. The pH value of the solution was adjusted to 1 by adding 9 M HCl. Afterward, the solution was transferred to a teflon-lined stainless-steel autoclave, sealed, and maintained at 200 °C for 12 h. The obtained precipitate was washed with water and centrifugated 3 times. Afterwards, the product was collected and dried in vacuum at 70 °C for 12 h. The product is denoted as MoO_2/PDDA/V_2C-1 or MoO_2/PDDA/V_2C-2, based on the mass ratio of the molybdenum source to V_2C (8:1 or 4:1), respectively. The products were annealed at 400 °C with argon flow for 2 h. The annealed samples were collected and marked as $MoO_2/C/V_2C$-1 or $MoO_2/C/V_2C$-2 according to the mass ratio of the molybdenum source to V_2C (8:1 or 4:1), respectively.

2.2. *Synthesis of $MoO_2/C/V_2C$ and MoO_2/PDDA composites*

The MoO_3/V_2C and MoO_2/PDDA composites were synthesized with the same procedure as the MoO_2/PDDA/V_2C composites except for the addition of PDDA and V_2C-MXene, respectively. The MoO_3/V_2C and MoO_2/PDDA products were annealed at 400 °C with an argon flow for 2 h and denoted as MoO_3/V_2C (annealed) and MoO_2/C (annealed).

2.3. *Material characterization*

X-ray diffraction (XRD) measurements were conducted on a Bruker AXS D8 Advance Eco diffractometer using Cu K_α radiation with a step size of $\Delta(2\Theta) = 0.02°$ Scanning Electron Microscopy (SEM), Transmission Electron Microscopy (TEM) and high-resolution TEM (HRTEM) were performed using a ZEISS Leo 1530 SEM and a Tecnai F30 TEM (FEI Corporation, USA) at an acceleration voltage of 200 kV, respectively, to study the morphology of the materials. Elemental mapping was performed on a Scanning Transmission Electron Microscope (STEM) unit with a high-angle annular dark-field (HAADF) detector (FEI, Tecnai F30), operating at an acceleration voltage of 200 kV. X-ray photoelectron spectroscopy (XPS) measurements were conducted using a MAX 200 (Leybold-Heraeus) spectrometer equipped with a hemispherical analyzer (EA 200; Leybold-Heraeus) and a Mg Kα X-ray source. The XP spectra were acquired in normal emission geometry with an energy resolution of ~0.9 eV. The binding energy (BE) scale of the spectra was referenced to the Au $4f_{7/2}$ peak at 84.0 eV.

2.4. *Battery assembly and electrochemical measurements*

To prepare the working electrodes, the active material (V_2C-MXene composite) was mixed with carbon black and polyvinylidene difluoride (PVDF, Solvay Plastics) at a mass ratio of 7:2:1 and dissolved in 1-methyl-2-pyrrolidone (NMP, Sigma Aldrich) by magnetic stirring for at least 12 h[27]. After removing most NMP in vacuum, the mixed slurry was then applied on circular Cu meshes (diameter 10 mm for the measurements inside the coin cell and 16 mm for the EL-CELL). The prepared electrodes were then dried at 80 °C under vacuum, mechanically pressed at 10 MPa, and then dried again, which resulted in an average mass loading of the electrodes of about 2–3 mg cm^{-2}[28]. The electrochemical performance of the fabricated electrodes was evaluated using coin cells (type 2032). A three-electrode PAT-Cell from EL-CELL was used for potentiostatic electrochemical impedance measurements (PEIS) [29]. For the coin cell preparation, two layers of glass microfibre separator (WhatmanGF/D) soaked with 130 µl of a 1 M solution of $LiPF_6$ in ethylene carbonate (EC)/dimethyl carbonate (DMC; 1:1 by volume; LP30, Merck) and a lithium foil (Sigma Aldrich) pressed on a nickel plate were used. All cell assemblies were performed in a glove box under argon atmosphere ($O_2/H_2O < 0.1$ ppm). All electrochemical measurements were carried in the voltage range from 0.01 to 3 V with a VMP3 potentiostat (BioLogic) at room temperature. For the PEIS measurements, the small disturbance of 10 mV in the frequency range from 200 kHz to 1 mHz was selected. To ensure time invariance of the measurement as well as a steady state, a 24 h OVC (open circuit voltage) was

performed before the PEIS measurement, and a second control PEIS measurement was carried out directly afterwards.

3. Results and discussion

3.1.1. *Morphology and structure of $MoO_2/C/V_2C$-1 and $MoO_2/C/V_2C$-2 composites*

The synthesis procedure of $MoO_2/C/V_2C$ composites is shown in Fig. 1a. Firstly, multilayer V_2C-MXene was synthesized via an etching process with a mixed solution of HCl and LiF from commercial V_2AlC. Next, PDDA, a typical cationic polyelectrolyte in aqueous solution, was introduced. The subsequent combination of PDDA and V_2C by the electrostatic force leads to two advantageous effects: firstly, the V_2C dispersion is stabilized in aqueous solution and, secondly, for the subsequent treatment, V_2C becomes positively charged on the surface. The stability of the synthesized multilayer V_2C-MXene and V_2C/PDDA dispersions in water was evaluated (Fig. 1b-d). After 12 h, most V_2C-MXene agglomerated and precipitated, and very little V_2C was dispersed, demonstrating the poor aqueous dispersibility of multilayer V_2C-MXene (right in Fig. 1b). In contrast, the presence of PDDA in V_2C/PDDA stabilizes the V_2C-MXene in an aqueous solution via electrostatic interaction, resulting in enhanced aqueous dispersibility of V_2C/PDDA (left in Fig. 1b). The stability of dispersion was maintained even after 48 and 72 h (Fig. 1c, d). This improvement makes it possible to preserve the hierarchical structure from multilayer V_2C-MXene and integrate it with MoO_2 for high-performance lithium storage. Next, the positively charged V_2C/PDDA was combined with isopolymolybdate anions $Mo_7O_{24}^{6-}$ from the molybdenum source $(NH_4)_6Mo_7O_{24}$ by electrostatic interaction[30,31]. After the hydrothermal reaction, the MoO_2/PDDA/V_2C-1 and MoO_2/PDDA/V_2C-2 composites, based on the mass ratio of the molybdenum source to V_2C (8:1 or 4:1), respectively, were obtained. The composites were then converted to $MoO_2/C/V_2C$-1 and $MoO_2/C/V_2C$-2 via an annealing process.

The crystal structure and phase characteristics of composites and precursors are determined by XRD as shown in Fig. 2 and Figures S1, S2, respectively. After the etching process, the diffraction peaks corresponding to V_2AlC significantly weaken and the new peak at 8.7° (Figure S1) ascribed to the interlayer ordering of the (002) planes of V_2C shows the successful preparation of MXene[32,33]. The appearance of extra diffraction peaks neither ascribed to the MAX nor the MXene phase can be related to the impurity phase of Li_3AlF_6, which is formed during the etching process[34]. In the XRD patterns of the MoO_2/PDDA/V_2C-1 and MoO_2/PDDA/V_2C-2 composites (Fig. 2), the V_2C (002) diffraction peak shifts to 8.2° indicating an enlarged interlayer distance after the formation of the composites[35,36]. Besides, strong diffraction peaks at 26.2°, 36.8° and 53.6° are observed, which can be ascribed to the (110), (111) and (220) peaks of monoclinic MoO_2 (ICSD code 80,830) [37]. After the annealing process, the MoO_2 phase is maintained, and weak diffraction peaks at around 22.4°, 23.7° and 33.6° signal the presence of $MoO_{2.75}$ in $MoO_2/C/V_2C$-1 and $MoO_2/C/V_2C$-2[38]. Note the absence of the (002) peak associated with the V_2C-MXene structure, which has also been reported in other works[20,31]. It might be the effect of the annealing process at high temperatures and indicates the lack of interlayer order in the formed V_2C-MXene. Additionally, compared to $MoO_2/C/V_2C$-1, the XRD pattern of $MoO_2/C/V_2C$-2 exhibits broader MoO_2 diffraction peaks, which suggests poorer crystallinity or smaller crystallite sizes of the oxide subsystem. One might speculate that the higher content of V_2C-MXene in the $MoO_2/C/V_2C$-2 composite leads to an increased depletion of the lattice oxygen atoms at high temperatures and hence results in this effect[39]. The synthesis process without the addition of V_2C-MXene leads to the production of MoO_2/PDDA and corresponding annealing to MoO_2/C. The XRD patterns of these materials exhibit distinct diffraction peaks, which closely match those of monoclinic MoO_2 (Fig. S2a). On this basis, we conclude that PDDA also works as a reducing agent during the hydrothermal reaction. Consistently, the absence of PDDA results in the production of mixed phases of h-MoO_3 and α-MoO_3 in MoO_3/V_2C and the annealed MoO_3/V_2C composites (see Figure S2b). Moreover, the diffraction peak at 8.2° ascribed to the (002) plane of V_2C vanishes after the annealing process, which is in line with the findings for $MoO_2/C/V_2C$.

SEM, TEM, HRTEM, and HRTEM energy dispersive spectroscopy (HRTEM-EDS) measurements were performed to investigate the morphology and the elemental distribution of the samples. As shown in Fig. 3a, compared to the densely packed V_2AlC (Figure S3), the synthesized V_2C exhibits the typical accordion-like morphology of MXenes with the multilayer structure. The framework given by this open structure promises to provide sufficient channels for electrolyte penetration and to reduce the migration pathway for lithium ions[40,41]. The SEM images of the $MoO_2/C/V_2C$-1 composite (Fig. 3b) show that MoO_2 nanoparticles are distributed uniformly in and on the layered structure. The hierarchical structure in this composite is not clearly visible due to the presence of excessive MoO_2. By comparison, the smaller amount of MoO_2 in $MoO_2/C/V_2C$-2 allows to identify a more obvious hierarchical structure (Fig. 3c). To estimate the size and morphology of the formed MoO_2, a view on the annealed MoO_2/C composite shows a MoO_2 morphology of micro particles with a size of 10–20 μm (Figure S4). The fact that the rational design with PDDA is indispensable for an improved

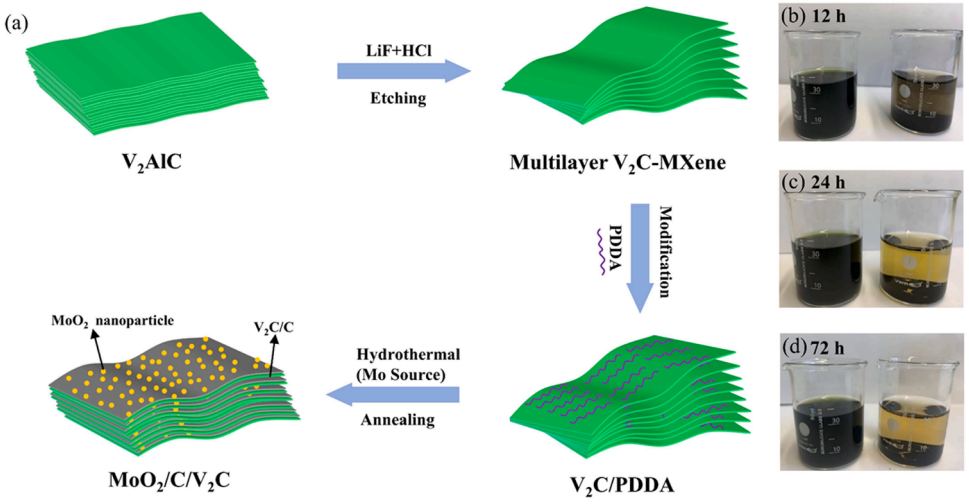

Fig. 1. (a) Schematic illustration of the preparation of $MoO_2/C/V_2C$ composites. The right panel shows photographs of dispersions of pristine V_2C-MXene (right beakers) and V_2C/PDDA (left beakers) in water after 12 h (b), 24 h (c), and 72 h (d).

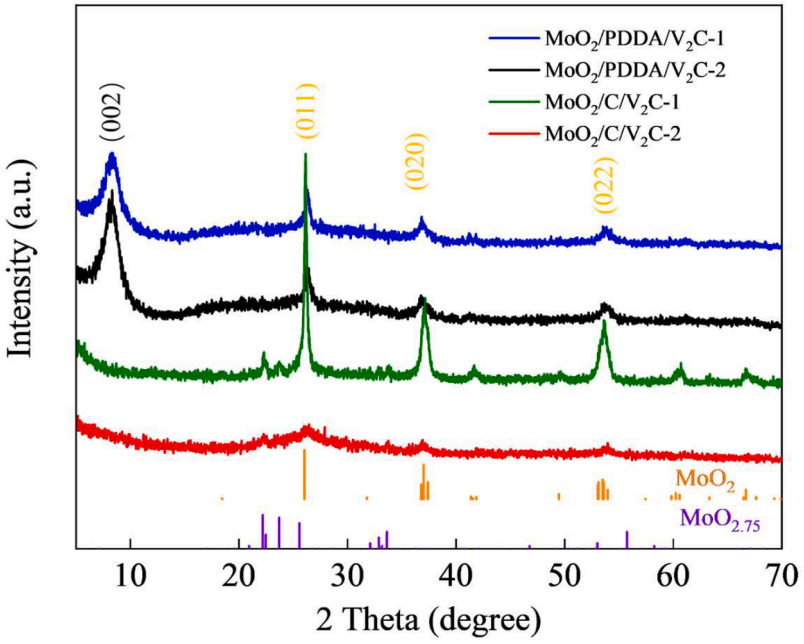

Fig. 2. XRD patterns of MoO_2/PDDA/V_2C-1, MoO_2/PDDA/V_2C-2, MoO_2/C/V_2C-1, and MoO_2/C/V_2C-2. Vertical ticks represent the reference patterns of MoO_2 and $MoO_{2.75}$ according to ICSD codes 80,830 and 201,573, respectively. The black (002) label and the analogous yellow labels related to interplanar ordering in the MXene and MoO_2 diffraction peaks, respectively.

combination of V_2C-MXene with MoO_2 is proven by the SEM images of the obtained MoO_3/V_2C (annealed) material (Figure S5), where only a mixture of MoO_3 micro rods and accordion-like V_2C is seen. This demonstrates that the layered structure of V_2C-MXene cannot be effectively utilized to confine MoO_2 without the addition of PDDA. TEM images of MoO_2/C/V_2C-1 in Fig. 3d-f are in agreement with the SEM results and show a hierarchical structure, where MoO_2 nanoparticles of a size of around 20 nm are almost uniformly confined in the amorphous V_2C/C matrix. The HRTEM image of MoO_2/C/V_2C-1 shows a lattice spacing of 0.34 nm corresponding to the (110) plane of monoclinic MoO_2 (Fig. 3 g), which is in accordance with the XRD results. HRTEM-EDS mapping (Figs. 3i-l) of the selected area in Fig. 3h (red rectangle) confirms the homogeneous distribution of Mo, O, V, and C, indicating sufficient loading of MoO_2 nanoparticles in this hierarchical composite.

The TEM images of MoO_2/C/V_2C-2 (Fig. 4a-c) show a similar hierarchical structure of MoO_2 nanoparticles constrained in the V_2C/C framework. Here, the MoO_2 nanoparticles (Fig. 4d) exhibit smaller sizes (~1–2 nm) than in MoO_2/C/V_2C-1, but also, in accordance with the XRD results, a poorer crystallinity. The uniform distribution of Mo, O, V, and C is verified by the HRTEM-EDS mapping of MoO_2/C/V_2C-2 in Figs. 4e-i.

Chemical states and compositions of V_2C-MXene, MoO_2/C/V_2C-1 and MoO_2/C/V_2C-2 were investigated by XPS. The wide-scan spectra of MoO_2/C/V_2C-1 and MoO_2/C/V_2C-2 shown in Figure S6 confirm the presence of Mo, O, V, and C in these composites in agreement with the results of the EDS elemental mapping. In the case of V_2C-MXene, V, C, and O can be observed. The detected O 1 s can be assigned to the O-related termination as well as vanadium oxides on V_2C-MXene[42]. The V 2p XP spectrum of V_2C-MXene shown in Fig. 5b exhibits a superposition of two V $2p_{3/2,1/2}$ doublets and an O satellite peak. The first doublet, with the component peaks at ~513.4 and ~519.6 eV, corresponds to V^{2+}($V-C$ bond). The second doublet, with the component peaks at ~516.1 and ~523.4 eV, is assigned to V^{4+}, resulting from the surface oxidation of V_2C-MXene[19,43]. The C 1 s XP spectrum of the V_2C-MXene shown in Fig. 5c reveals the coexistence of four characteristic peaks at 282.1, 284.8, 287.6 and 290.1 eV corresponding to $C-V$, $C-C$, $C-O$ and $O-C{=}O$ bonds, respectively[43,44]. The above results confirm the successful preparation of V_2C.

For MoO_2/C/V_2C-1 and MoO_2/C/V_2C-2, the characteristic peaks ascribed to C—V and O—C=O bonds vanish, and the peak related to C—C becomes dominant in the C 1 s XP spectra. Moreover, only one weak doublet assigned to V^{4+} is visible in the V 2p XP spectra. A possible explanation for this is that the MXene structure (as seen in the SEM and TEM data for the MoO_2/C/V_2C composites) is more or less fully hidden behind the layer of MoO_2 nanoparticles/amorphous carbon and therefore not detectable by the surface sensitive XPS[15,45]. The Mo 3d XP spectra of MoO_2/C/V_2C-1 and MoO_2/C/V_2C-2 exhibit three Mo $3d_{5/2,3/2}$ doublets. The doublet with the component peaks at 229.1 and 232.4 eV is, in good agreement with other reports, assigned to Mo^{4+}[23,46]. The other two doublets, with the component peaks at 232.4 and 235.5 eV, 230.9 and 233.8 eV, correspond to Mo^{6+} and Mo^{5+}, respectively, indicate slight surface oxidation of MoO_2[47,48].

3.2. *Lithium-ion storage in the MoO_2/C/V_2C-1 and MoO_2/C/V_2C-2 composites*

CV and GCPL measurements shown in Fig. 6 elucidate the electrochemical behavior and, in particular, the ability of the composite materials under study to store lithium-ions. Figs. 6a, b present CV curves of the MoO_2/C/V_2C-1- and MoO_2/C/V_2C-2-based electrodes, respectively, obtained at a scan rate of 0.1 mV/s in the voltage range 0.01–3 V. The observed peaks show the fingerprints of the electrochemical reactions, including those in the MoO_2 subsystem, which can be summarized as following[49]:

$$xLi^+ + xe^- + MoO_2 \leftrightarrow Li_xMoO_2 \ (0 < x < 0.98) \quad (1)$$

$$MoO_2 + (4-x)Li^+ + (4-x)e^- \leftrightarrow 2Li_2O + Mo \quad (2)$$

As seen in Fig. 6a, the first cathodic sweep displays two distinct reduction peaks at 1.6 V and 1.3 V. These peaks correspond to the two-step lithium insertion into MoO_2 (Eq. (1)), during which the phase of MoO_2 transforms from monoclinic to orthorhombic and back to monoclinic[24,50]. The reduction peak at 0.7 V can be ascribed to the formation of SEI, which is absent in the subsequent cycles[39]. Another reduction peak at around 0.4 V represents the conversion reaction from Li_xMoO_2 to metallic molybdenum (Eq. (2)) [49]. Additionally, several reduction peaks at the potential over 2 V are visible, which disappear in

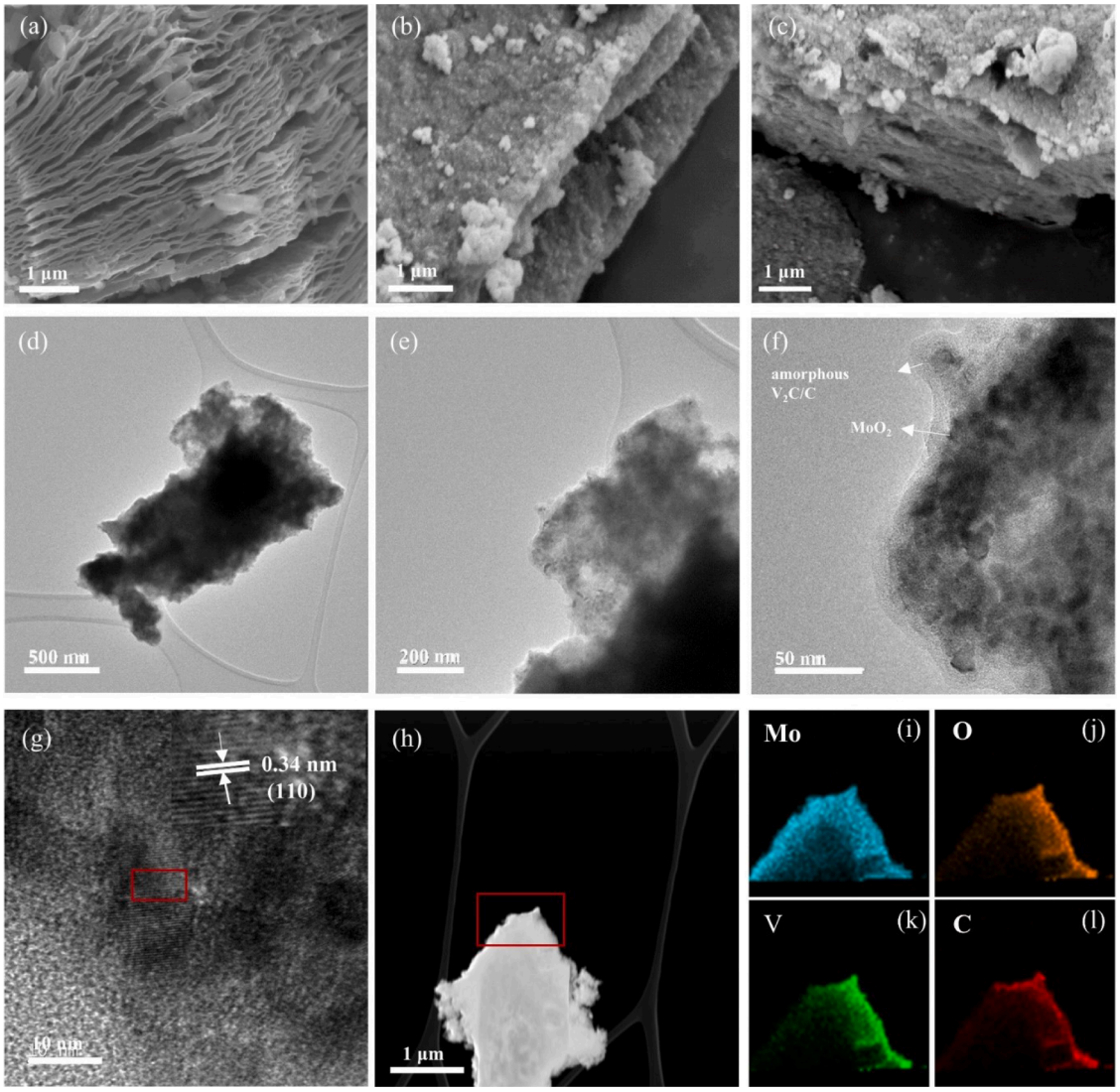

Fig. 3. SEM images of V_2C (a), $MoO_2/C/V_2C$-1 (b), and $MoO_2/C/V_2C$-2 (c). TEM images (d-f), HAADF-STEM image (g), and HAADF-STEM-EDS mapping (h-l) of $MoO_2/C/V_2C$-1.

the following cycles and therefore indicate irreversible reactions. A part of these irreversible reactions might be caused by traces of MoO_3, which originated from the partial oxidation in air on the surface of composites [51]. For the first anodic scan, two rather distinct oxidation peaks at 1.4 V and 1.7 V are observed on the background of enhanced electrochemical activity at ~1–2.2 V. The peaks are attributed to the Li_xMoO_2 delithiation process (Eq. (1)) [52]. In the second cathodic sweep, the two reduction peaks related to lithium insertion at 1.6 and 1.3 V are unchanged. The reduction peak related to the conversion reaction (Eq. (2)) at 0.15 V shows a potential shift compared with the first cycle. This is commonly observed in MoO_2-based electrodes and attributed to structural change during the conversion reaction[53]. Moreover, the increase in current density indicates a more complete conversion reaction and suggests the appearance of a known electrode activation effect[54]. The peaks in the second and fifth cycles are nearly overlapping, which implies good reversibility of the insertion and extraction of lithium ions.

The CV of $MoO_2/C/V_2C$-2 show a different behavior than those of $MoO_2/C/V_2C$-1, in particular the absence of the distinct feature associated with the processes described by Eqs (1) and (2), which can be partly explained by the lower MoO_2 content in the former composite material. Starting again with the first cathodic scan, the irreversible reduction peak at 2.7 V likely signals small electrochemical activity of MoO_3, similar to that in the $MoO_2/C/V_2C$-1 electrode and in agreement with the existence of Mo^{6+} in the composite as demonstrated by the XPS data. The broad peak at around 1.26 V corresponds to the lithiation of MoO_2 to Li_xMoO_2, the broad width of which is explained by the amorphous structure of the MoO_2 nanoparticles in $MoO_2/C/V_2C$-2[33]. The broad reduction peak at 0.6 V indicates the formation of SEI and the conversion reaction of Li_xMoO_2. In contrast to $MoO_2/C/V_2C$-1, only one oxidation peak at 1.52 V attributed to the delithiation process is observed during the first anodic scan. Upon further cycling, the CV profiles remain fairly consistent and steady in the fifth cycle, suggesting good reversibility and stability of lithium-ion transport.

The galvanostatic charge/discharge curves of both the $MoO_2/C/V_2C$-1 and $MoO_2/C/V_2C$-2 electrodes at a current density of 100 mA g^{-1} are shown in Figure S7. The $MoO_2/C/V_2C$-1 electrode delivers an initial discharge/charge capacity of 875/496 mAh g^{-1} with an initial Coulombic efficiency of 57% (Figure S7a). The capacity loss arises from SEI formation and the irreversible reaction(s) at high potential (>2.5 V). There are two faint plateaus at around 1.3 and 1.6 V in agreement with the CV curves. In contrast, a higher first cycle Coulombic efficiency of around 70% is achieved for the $MoO_2/C/V_2C$-2 electrode (Figure S7b), which exhibits an initial discharge/charge capacity of 1190/840 mAh g^{-1}, thereby indicating a better synergistic effect of the components.

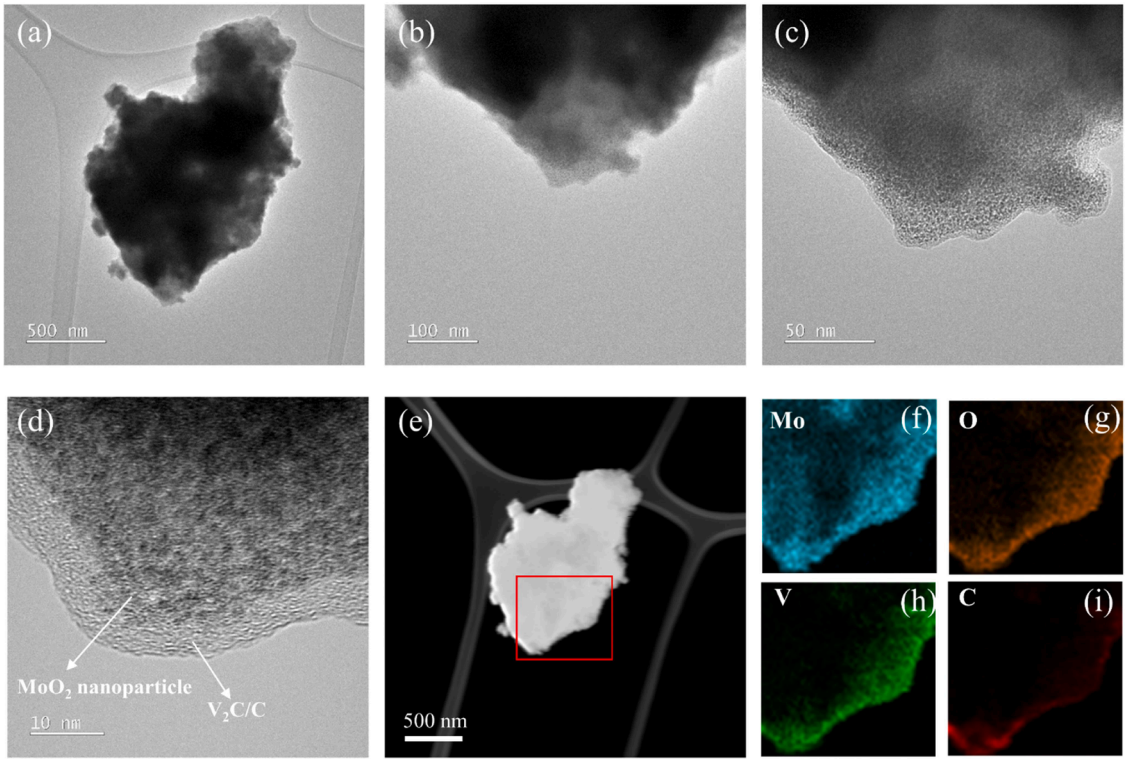

Fig. 4. TEM images (a-c), HRTEM image (d), and HRTEM-EDS mapping (e-i) of $MoO_2/C/V_2C$-2.

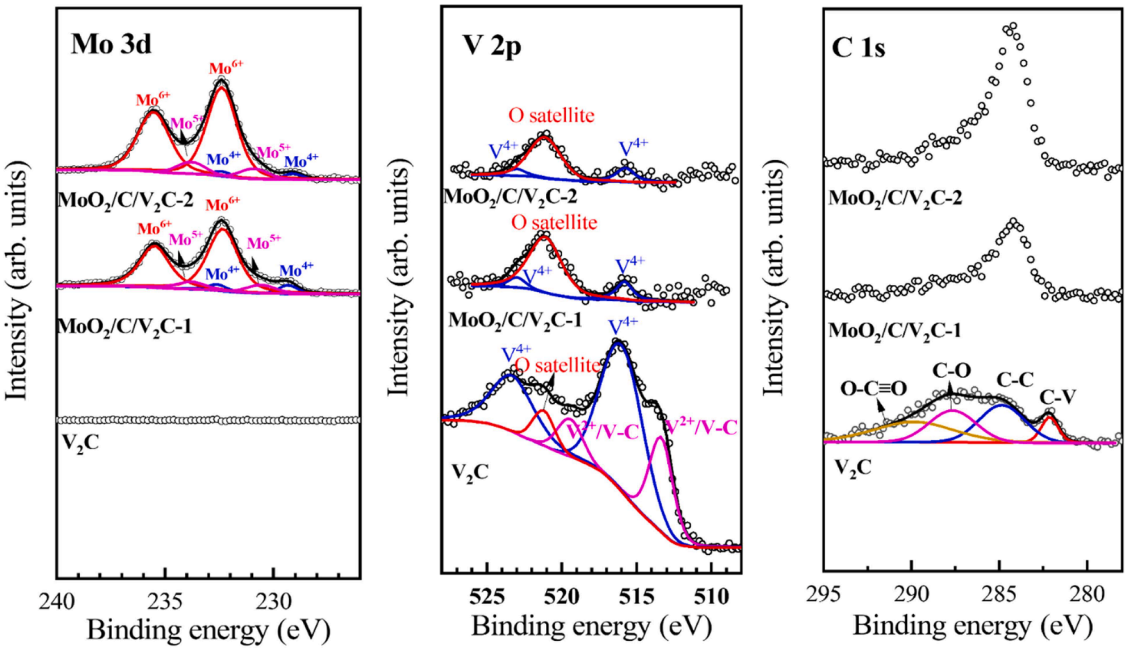

Fig. 5. Mo 3d (a), V 2p (b), and C 1 s XP spectra of V_2C-MXene, $MoO_2/C/V_2C$-1, and $MoO_2/C/V_2C$-2.

Fig. 6c shows the cycling performance of the $MoO_2/C/V_2C$-1 and $MoO_2/C/V_2C$-2 electrodes at a current density of 100 mA g^{-1} for 100 cycles. The corresponding data for pristine V_2C, MoO_2/PDDA/V_2C-1 and MoO_2/PDDA/V_2C-2 are also presented for comparison. The pristine V_2C electrode exhibits good capacity stability but features only low reversible capacity of 196 mAh g^{-1} after 100 cycles. In this pristine MXene, the performance is known to be limited by the lithium-ion insertion mechanism and the existence of surface groups[55,56]. By comparison, the MoO_2/PDDA/V_2C-1 and MoO_2/PDDA/V_2C-2 electrodes show higher initial discharge/charge capacities but a fast drop to 170–180 mAh g^{-1} in the first 15 cycles. We attribute this strong fading to poor electrochemical behavior of PDDA in these two composites, which diminishes the lithium storage performance of MoO_2 [57]. This problem can be overcome by converting PDDA to amorphous carbon via an annealing process as evidenced by the cycling performance of our $MoO_2/C/V_2C$-1 and $MoO_2/C/V_2C$-2 electrodes. Both electrodes exhibit enhanced lithium-ion storage performance compared to their untreated counterparts. As shown in Fig. 6c, the $MoO_2/C/V_2C$-1 electrode shows a slight

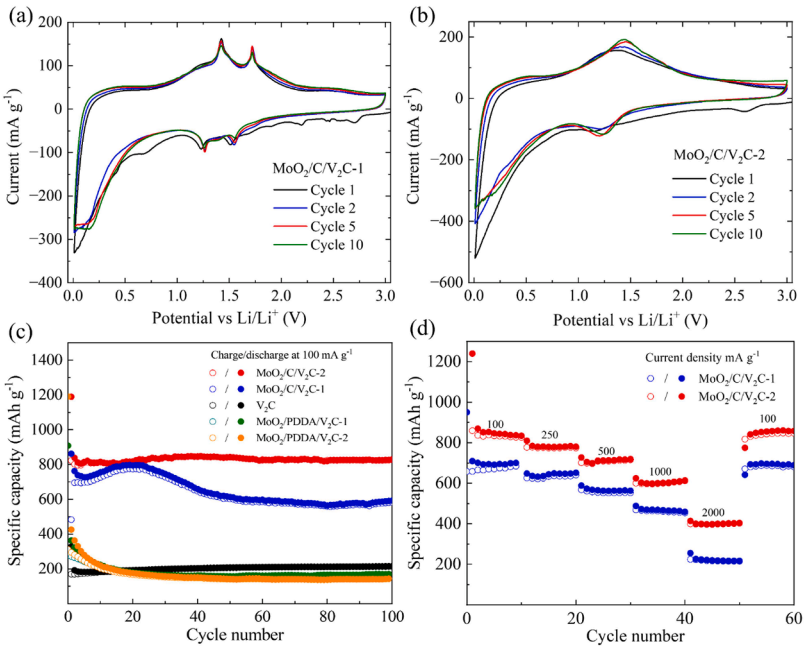

Fig. 6. CV curves for the (a) $MoO_2/C/V_2C$-1 and (b) $MoO_2/C/V_2C$-2 electrodes for the first, second, and fifth cycle at a scan rate of 0.1 mV s^{-1} and in a potential range of 0.01–3 V vs. Li/Li^+. (c) Cycling performance at 100 mA g^{-1} and (d) rate performance at the current densities ranging from 100 to 2000 mA g^{-1}. In (c), the electrochemical performance of V_2C-MXene, MoO_2/PDDA/V_2C-1 and MoO_2/PDDA/V_2C-2 are also shown for comparison.

capacity increase in the first 20 cycles, which is however followed by clear capacity fading in the next 20 cycles. Afterwards, the capacity is maintained in the subsequent 60 cycles. The capacity increase can be attributed to the progressive conversion reaction known as the electrode activation effect, where the produced metallic Mo activates more Li_x-MoO_2 to participate in the conversion reaction[54]. However, the aggregation of metallic Mo to form metal clusters would hinder this activation effect, causing a capacity drop. The good electrical contacts provided by constructing hierarchical structures with materials like graphene[53] and MXene, as shown here, can alleviate the aggregation and stabilize the cycling process. In the case of the $MoO_2/C/V_2C$-2 electrode, the amorphous structure of MoO_2 and the higher amount of MXene in the composites offer more complete conversion reactions and a better confinement effect. Compared to $MoO_2/C/V_2C$-1 this results in a drastically improved capacity retention of 99% (a reversible capacity of 810 mAh g^{-1}) after 100 cycles. Without the unique hierarchical structure, the synthesized annealed MoO_2/C and MoO_3/V_2C samples show fast capacity degradation and specific capacities of only 352 and 315

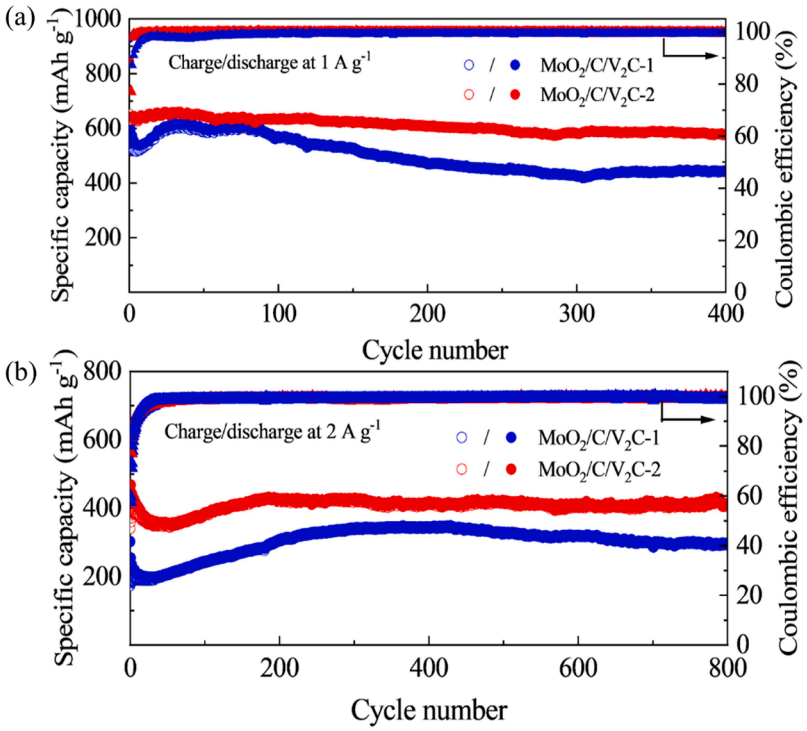

Fig. 7. Long-term cycling performance and Coulombic efficiency of $MoO_2/C/V_2C$-1 and $MoO_2/C/V_2C$-2 at high current densities of (a) 1000 and (b) 2000 mA g^{-1}.

mAh g^{-1} are retained after 100 cycles (Figures S8 and S9).

The rate capabilities of the $MoO_2/C/V_2C$-1 and $MoO_2/C/V_2C$-2 electrodes were also tested under different current densities ranging from 100 to 250, 500, 1000 and 2000 mA g^{-1} (see Fig. 6d). The $MoO_2/C/V_2C$-1 electrode delivers average specific discharge/charge capacities of 692, 638, 559, 446, and 224 mAh g^{-1}, respectively. As the current density is returned to 100 mAg^{-1}, the specific discharge/charge capacity quickly recovers to 670 mAh g^{-1}. Similar but superior rate performance is observed for the $MoO_2/C/V_2C$-2 electrode, which shows higher average specific discharge/charge capacities of 840, 782, 714, 603 and 401 mAh g^{-1}, respectively, at the same current densities. Consequently, both electrodes display high reversibility and outstanding rate capability, benefiting from the enhanced conductivity and the unique hierarchical structure of the $MoO_2/C/V_2C$ composites.

Inspired by the outstanding cycling stabilities and rate capabilities of the $MoO_2/C/V_2C$-1 and $MoO_2/C/V_2C$-2 electrodes, the long cycling capability of the above two electrodes at a high current density of 1000 and 2000 mA g^{-1} was investigated. As shown in Fig. 7a, the $MoO_2/C/V_2C$-1 and $MoO_2/C/V_2C$-2 electrodes exhibit reversible capacities of 420 and 603 mAh g^{-1}, respectively, after 400 cycles at a current density of 1000 mA g^{-1}. Moreover, for these electrodes, capacities of 294 and 412 mAh g^{-1} can still be achieved after 800 cycles at a high current density of 2000 mA g^{-1}, implying excellent long-term cycling stability. The initial capacity reduction followed by gradual increase at 2 A/g (Fig. 7) may stem from two key factors: 1) kinetic Limitations: High current density (2 A/g) initially hinders full Li^+diffusion into the $MoO_2/C/V_2C$ composite, causing incomplete conversion reactions and irreversible Li^+ consumption for metastable SEI formation. 2) Progressive Activation: with cycling, the hierarchical V_2C/C framework enables gradual optimization of ionic/electronic pathways (supported by EIS in Fig. 8a), while confined MoO_2 nanoparticles achieve enhanced conversion reactivity ($MoO_2 \rightleftharpoons Mo + Li_2O$), aligning with the delayed capacity rise observed in MoO_2/graphene systems[53].

To examine the kinetics and supposed kinetic disparities between $MoO_2/C/V_2C$-1 and $MoO_2/C/V_2C$-2, potentiostatic electrochemical impedance measurements (PEIS) were conducted. The resultant Nyquist plots, alongside the fits obtained using the Z Fit function of the EC-Lab (Bio-Logic) software, are depicted in Fig. 8a. These plots exhibit a depressed semi-circle in the high to medium frequency range, reflecting the charge transfer resistance followed by a steep rise in the low-frequency range, indicative of Li^+ diffusion impedance. Quantitative analysis, accomplished by fitting the data with the corresponding equivalent circuit (see equivalent circuit depicted in Fig. 8a), allows to assess parameters such as electrolyte resistance (R_e), charge transfer resistance between the electrolyte and electrode material (R_{ct}), and double-layer capacitance (C_{dl}). Our analysis yields an electrolyte resistance of 2.5(8) Ω for $MoO_2/C/V_2C$-2 and 1.7(3) Ω for $MoO_2/C/V_2C$-1, and a rather small charge transfer resistance of 109(1) Ω and 133(1) Ω, as well as double layer capacity of 2.29(8) μF and 2.09(3) μF, respectively. The better high current capability (see Figure. 6) and the also in comparison lower charge transfer resistance values clearly display that $MoO_2/C/V_2C$-2 exhibits faster kinetics than $MoO_2/C/V_2C$-1. The faster kinetics likely originates from a better synergistic effect between the components in this composite and allows the conclusion that the MoO_2 to MXene ratio for fast kinetics and better electrochemical performance should rather be in the range of 4:1 than in the range of 8:1. More significantly, as depicted in Fig. 8b, the long-term cycling performance and rate capabilities of the $MoO_2/C/V_2C$ composites notably exceed most previously reported for both MXene-based composites and MoO_2 composite anode materials. Our systematic study of the different electrode materials allows us to ascribe the superior battery performance of the here reported $MoO_2/C/V_2C$ composites to the following two properties: (1) The unique hierarchical structure strongly suppressing capacity fading, and (2) the V_2C/C framework enhancing the electric conductivity of the composites, thereby improving the kinetics of the electrochemical processes. This is straightforwardly attributed to the proper confinement of the MoO_2 nanoparticles to accommodate the volume expansion during cycling and to alleviate metallic Mo aggregation. In addition, the hierarchical confinement structure provides full contact between electrode and electrolyte. Compared to well-established anode materials such as graphite and silicon-based counterparts, the current challenges of the $MoO_2/C/V_2C$ composite primarily lie in the relatively high cost of raw materials (e.g., V_2C MXene) its environmental -unfriendly synthesis processes synthesis process. However, the hydrothermal method followed by annealing, as proposed in this work, offers a simplified and scalable preparation route for the $MoO_2/C/V_2C$ composite. We acknowledge that further cost reduction of MXene materials and optimization of synthesis method are essential for large-scale production. Nevertheless, with the rapid development of MXene manufacturing technologies and economies of scale, we believe this composite holds promising potential for practical applications in next-generation lithium-ion batteries.

(a)

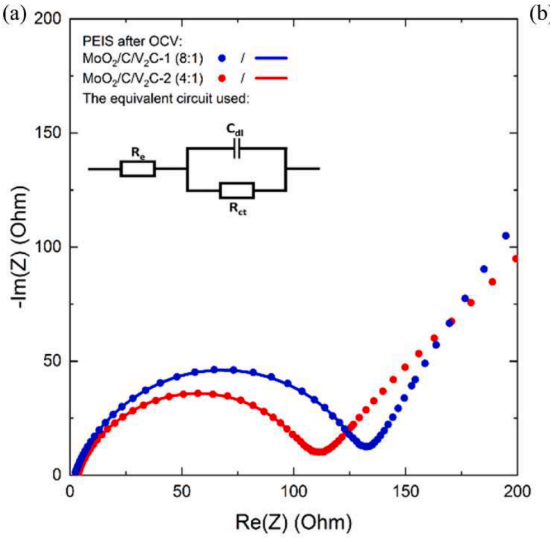

(b)

Electrode	current density (mA/g)	Reversible capacity (mAh/g)	cycle number	Ref.
porous MoO_2/graphene	100	1300	100	[23]
MoO_2/N-doped MCNTs	1000	507.8	500	[26]
MoO_2/C Nanospheres–Porous Graphene Composites	1000	642	500	[39]
MoO_2/C	100	400	60	[53]
MoO_2/Carbon Microflowers	500	690	200	[51]
MoO_2/C	80	1113	60	[52]
MoS_2/Ti_3C_2	100	509	100	[17]
SnS/Ti_3C_2	100	646	100	[20]
SnO_x/Ti_3C_2	500	540	1000	[35]
Sn/Ti_3C_2	200	226.2	1000	[58]
SiO_2/Ti_3C_2	265	1092	378	[59]
Mo_3Se_4/Ti_3C_2	1000	635	200	[60]
MoS_2/C@Ti_3C_2	1000	600	700	[61]
Bi_2S_3 nanoroll/Ti_3C_2	1000	541	600	[62]
$MoO_2/C/V_2C$	**1000** **2000**	**603** **412**	**400** **800**	**This work**

Fig. 8. (a) Nyquist plots for $MoO_2/C/V_2C$-1 and $MoO_2/C/V_2C$-2 measured after OCV. Solid lines display fits according to the equivalent circuit shown in the inset. (b) Comparison of the cycling performance at various current densities for the $MoO_2/C/V_2C$ composites with those of the recently reported MXene-based composites and MoO_2 composite anode materials [17,20,23,26,35,39,51–53,58–62].

4. Conclusions

We report on the successful preparation of $MoO_2/C/V_2C$ composites by an electrostatic interaction-assisted hydrothermal and a post-annealing process. In our process, the problem of the V_2C dispersion in water is solved through the introduction of PDDA, providing the possibility to prepare highly functional composites of V_2C with MoO_2. As a result, our composite features MoO_2 nanoparticles confined in the layered framework of V_2C/C, derived from V_2C/PDDA. Benefitting from this unique hierarchical structure, the $MoO_2/C/V_2C$ composites exhibit outstanding lithium storage performance. The two MoO_2/V_2C/C-based electrodes with different MoO_2/V_2C ratios show reversible specific capacities of 602 and 810 mAh g^{-1}, respectively, at 100 mA g^{-1} after 100 cycles. In particular, the two composites also exhibit superior long-term cycling performance with reversible capacities of 292 and 412 mAh g^{-1} at a high current density of 2000 mA g^{-1} after 750 cycles. Moreover, excellent rate performance is obtained for the electrodes of these two composites. The data also suggest that the MoO_2:V_2C ratio and the size and crystallinity of MoO_2 nanoparticles are important to further optimize the performance of the hierarchical composite materials. Notably, the design strategy and the synthesis route have great potential to be extended to construct other remarkable composites based on unexfoliated multilayer MXene as host framework in combination with high capacity conversion-/alloy-type materials.

CRediT authorship contribution statement

Peng Guo: Writing – review & editing, Writing – original draft, Project administration, Methodology, Investigation, Formal analysis, Data curation, Conceptualization. **Lennart Singer:** Writing – review & editing, Methodology, Investigation. **Zhiyong Zhao:** Methodology, Investigation. **Brian Hinz:** Methodology, Investigation, Data curation. **Tomasz Kędzierski:** Methodology, Investigation, Data curation. **Tobias König:** Methodology, Investigation, Data curation. **Ewa Mijowska:** Writing – review & editing, Supervision, Project administration. **Michael Zharnikov:** Writing – review & editing, Supervision, Project administration, Methodology, Investigation. **Peter Comba:** Writing – review & editing, Supervision, Project administration, Conceptualization. **Rüdiger Klingeler:** Writing – review & editing, Supervision, Project administration, Funding acquisition, Data curation, Conceptualization.

Declaration of competing interest

The authors declare that they have no known competing financial interests or personal relationships that could have appeared to influence the work reported in this paper.

Acknowledgments

This work was partly supported by the Deutsche Forschungsgemeinschaft (DFG) via KL 1824/20-1 and by the DFG Research Training Group "Mixed Ionic Electronic Transport" (GRK 2948). G.P. acknowledges support through the China Scholarship Council (CSC). The authors thank I. Glass for experimental support. The authors also thank Prof. Jörg Pross and I. Glass for the HF lab support.

Supplementary materials

Supplementary material associated with this article can be found, in the online version, at doi:10.1016/j.electacta.2025.146413.

Data availability

No data was used for the research described in the article.

References

[1] M. Naguib, M. Kurtoglu, V. Presser, J. Lu, J. Niu, M. Heon, L. Hultman, Y. Gogotsi, M.W. Barsoum, Two-dimensional nanocrystals produced by exfoliation of Ti_3AlC_2, Adv. Mater. 23 (2011) 4248–4253, https://doi.org/10.1002/adma.201102306.
[2] M. Naguib, V.N. Mochalin, M.W. Barsoum, Y. Gogotsi, 25th anniversary article: MXenes: a new family of two-dimensional materials, Adv. Mater. 26 (2014) 992–1005, https://doi.org/10.1002/adma.201304138.
[3] Z.W. Seh, K.D. Fredrickson, B. Anasori, J. Kibsgaard, A.L. Strickler, M. R. Lukatskaya, Y. Gogotsi, T.F. Jaramillo, A. Vojvodic, Two-dimensional molybdenum carbide (MXene) as an efficient electrocatalyst for hydrogen evolution, ACS Energy Lett. 1 (2016) 589–594, https://doi.org/10.1021/acsenergylett.6b00247.
[4] M.R. Lukatskaya, O. Mashtalir, C.E. Ren, Y. Dall'Agnese, P. Rozier, P.L. Taberna, M. Naguib, P. Simon, M.W. Barsoum, Y. Gogotsi, Cation intercalation and high volumetric capacitance of two-dimensional titanium carbide, Science 341 (2013) 1502–1505, https://doi.org/10.1126/science.1241488.
[5] A. Iqbal, J. Kwon, M.K. Kim, C.M. Koo, MXenes for electromagnetic interference shielding: experimental and theoretical perspectives, Mater. Today Adv. 9 (2021), https://doi.org/10.1016/j.mtadv.2020.100124.
[6] B. Anasori, M.R. Lukatskaya, Y. Gogotsi, 2D metal carbides and nitrides (MXenes) for energy storage, Nat. Rev. Mater. 2 (2017), https://doi.org/10.1038/natrevmats.2016.98.
[7] M. Naguib, O. Mashtalir, J. Carle, V. Presser, J. Lu, L. Hultman, Y. Gogotsi, M.W.J. A.n. Barsoum, Two-dimensional transition metal carbides, ACS Nano 6 (2012) 1322–1331, https://doi.org/10.1021/nn204153h.
[8] H.T. Mathew, K. Abhisek, S.S. Vhatkar, R. Oraon, Headway towards contemporary 2D MXene-based hybrid electrodes for alkali-ion batteries, Energy Adv. 1 (2022) 950–979, https://doi.org/10.1039/d2ya00212d.
[9] H. Aghamohammadi, R. Eslami-Farsani, E. Castillo-Martinez, Recent trends in the development of MXenes and MXene-based composites as anode materials for Li-ion batteries, J. Energy Storage. 47 (2022), https://doi.org/10.1016/j.est.2021.103572.
[10] X. Tang, X. Guo, W. Wu, G. Wang, 2D Metal Carbides and Nitrides (MXenes) as High-Performance Electrode Materials for Lithium-Based Batteries, Adv. Energy Mater. 8 (2018), https://doi.org/10.1002/aenm.201801897.
[11] M. Naguib, J. Come, B. Dyatkin, V. Presser, P.-L. Taberna, P. Simon, M. W. Barsoum, Y. Gogotsi, MXene: a promising transition metal carbide anode for lithium-ion batteries, Electrochem. Commun. 16 (2012) 61–64, https://doi.org/10.1016/j.elecom.2012.01.002.
[12] M. Naguib, J. Halim, J. Lu, K.M. Cook, L. Hultman, Y. Gogotsi, M.W. Barsoum, New two-dimensional niobium and vanadium carbides as promising materials for Li-ion batteries, J. Am. Chem. Soc. 135 (2013) 15966–15969, https://doi.org/10.1021/ja405735d.
[13] R. Cheng, T. Hu, Z. Wang, J. Yang, R. Dai, W. Wang, C. Cui, Y. Liang, C. Zhang, C. Li, H. Wang, H. Lu, Z. Yang, H. Zhang, X. Wang, Understanding charge storage in Nb_2CT_x MXene as an anode material for lithium ion batteries, Phys. Chem. Chem. Phys. 23 (2021) 23173–23183, https://doi.org/10.1039/d1cp03070a.
[14] J. Jyoti, B.P. Singh, M. Sandhu, S.K. Tripathi, New insights on MXene and its advanced hybrid materials for lithium-ion batteries, Sustain. Energ. Fuels. 6 (2022) 971–1013, https://doi.org/10.1039/d1se01681d.
[15] Y. Wang, Y. Li, Z. Qiu, X. Wu, P. Zhou, T. Zhou, J. Zhao, Z. Miao, J. Zhou, S. Zhuo, Fe_3O_4@Ti_3C_2 MXene hybrids with ultrahigh volumetric capacity as an anode material for lithium-ion batteries, J. Mater. Chem. A. 6 (2018) 11189–11197, https://doi.org/10.1039/c8ta00122g.
[16] M. Zheng, R. Guo, Z. Liu, B. Wang, L. Meng, F. Li, T. Li, Y. Luo, MoS_2 intercalated p-Ti_3C_2 anode materials with sandwich-like three dimensional conductive networks for lithium-ion batteries, J. Alloys Compd. 735 (2018) 1262–1270, https://doi.org/10.1016/j.jallcom.2017.11.250.
[17] C. Chen, X. Xie, B. Anasori, A. Sarycheva, T. Makaryan, M. Zhao, P. Urbankowski, L. Miao, J. Jiang, Y. Gogotsi, MoS_2-on-MXene Heterostructures as Highly Reversible Anode Materials for Lithium-Ion Batteries, Angew. Chem. Int. Ed. 57 (2018) 1846–1850, https://doi.org/10.1002/anie.201710616.
[18] Z. Zhang, H. Ying, P. Huang, S. Zhang, Z. Zhang, T. Yang, W.-Q. Han, Porous Si decorated on MXene as free-standing anodes for lithium-ion batteries with enhanced diffusion properties and mechanical stability, Chem. Eng. J. 451 (2023), https://doi.org/10.1016/j.cej.2022.138785.
[19] T. Bashir, X. Li, S. Yang, Y. Song, S. Zhou, J. Wang, W. Zhu, J. Yang, J. Zhao, L. Gao, Enhancing role of structurally integrated V_2C MXene nanosh-eets on silicon anode for lithium storage, J. Alloys Compd. 922 (2022), https://doi.org/10.1016/j.jallcom.2022.166213.
[20] J. Ai, Y. Lei, S. Yang, C. Lai, Q. Xu, SnS nanoparticles anchored on Ti_3C_2 nanosheets matrix via electrostatic attraction method as novel anode for lithium ion batteries, Chem. Eng. J. 357 (2019) 150–158, https://doi.org/10.1016/j.cej.2018.09.109.
[21] W. Bi, G. Gao, C. Li, G. Wu, G. Cao, Synthesis, properties, and applications of MXenes and their composites for electrical energy storage, Prog. Mater. Sci. 142 (2024) 101227, https://doi.org/10.1016/j.pmatsci.2023.101227.
[22] A. Bhaskar, M. Deepa, T.N. Rao, U.V. Varadaraju, Enhanced nanoscale conduction capability of a MoO_2/Graphene composite for high performance anodes in lithium ion batteries, J. Pow. Sources. 216 (2012) 169–178, https://doi.org/10.1016/j.jpowsour.2012.05.050.
[23] K. Palanisamy, Y. Kim, H. Kim, J.M. Kim, W.-S. Yoon, Self-assembled porous MoO_2/graphene microspheres towards high performance anodes for lithium ion batteries, J. Power Sources. 275 (2015) 351–361, https://doi.org/10.1016/j.jpowsour.2014.11.001.

[24] S. Hu, F. Yin, E. Uchaker, W. Chen, M. Zhang, J. Zhou, Y. Qi, G. Cao, Facile and Green Preparation for the Formation of MoO_2-GO Composites as Anode Material for Lithium-Ion Batteries, J. Phys. Chem. C. 118 (2014) 24890–24897, https://doi.org/10.1021/jp508933c.
[25] Y. Zhou, Q. Liu, D. Liu, H. Xie, G. Wu, W. Huang, Y. Tian, Q. He, A. Khalil, Y. A. Haleem, T. Xiang, W. Chu, C. Zou, L. Song, Carbon-coated MoO_2 dispersed in three-dimensional graphene aerogel for lithium-ion battery, Electrochim. Acta. 174 (2015) 8–14, https://doi.org/10.1016/j.electacta.2015.05.153.
[26] Z. Wang, X. Chen, D. Wu, T. Zhang, G. Zhang, S. Chu, B. Qian, S. Tao, Strong metal oxide-support interaction in MoO_2/N-doped MCNTs heterostruc-ture for boosting lithium storage performance, J. Colloid Interface Sci. 650 (2023) 247–256, https://doi.org/10.1016/j.jcis.2023.06.192.
[27] P. Guo, L. Singer, Z. Zhao, W. Kukułka, F. Sebastian, E. Mijowska, M. Zharnikov, P. Comba, R. Klingeler, A facile preparation method and proof of cycle-stability of carbon-coated metal oxide and disulfide battery materials, Electrochim. Acta. 459 (2023) 142540, https://doi.org/10.1016/j.electacta.2023.142540.
[28] A. Ottmann, G. Zakharova, B. Ehrstein, R. Klingeler, Electrochemical performance of single crystal belt-like $NH_4V_3O_8$ as cathode material for lithium-ion batteries, Electrochim. Acta. 174 (2015) 682–687, https://doi.org/10.1016/j.electacta.2015.06.027.
[29] L. Singer, W. Kukułka, E. Thauer, N. Gräßler, A. Asyuda, M. Zharnikov, E. Mijowska, R. Klingeler, On the rising extra storage capacity of ultra-small Fe_3O_4 particles functionalized with HCS and their potential as high-performance anode material for electrochemical energy storage, Electrochimi. Acta. 448 (2023), https://doi.org/10.1016/j.electacta.2023.142155.
[30] X.W. Lou, H. Zeng, Hydrothermal synthesis of α-MoO_3 nanorods via acidification of ammonium heptamolybdate tetrahydrate, Chem. Mater. 14 (2002) 4781–4789, https://doi.org/10.1021/cm0206237.
[31] G. Liu, T. Zhang, X. Li, J. Li, N. Wu, A. Cao, W. Yuan, K. Pan, D. Guo, X. Liu, MoS_2@C with S vacancies vertically anchored on V_2C-MXene for efficient lithium and sodium storage, Inorganic Chem. Frontiers. 10 (2023) 1587–1602, https://doi.org/10.1039/d2qi02389j.
[32] F. Liu, J. Zhou, S. Wang, B. Wang, C. Shen, L. Wang, Q. Hu, Q. Huang, A. Zhou, Preparation of High-Purity V_2C MXene and Electrochemical Properties as Li-Ion Batteries, J. Electrochem. Soc. 164 (2017) A709–A713, https://doi.org/10.1149/2.0641704jes.
[33] M. Wu, Y. He, L. Wang, Q. Xia, A. Zhou, Synthesis and electrochemical properties of V_2C MXene by etching in opened/closed environments, J. Adv. Ceram. 9 (2020) 749–758, https://doi.org/10.1007/s40145-020-0411-8.
[34] A. Garg, A. Goel, S. Prasher, R. Kumar, R. Moulick, MXene nanocomposites for microwave absorption, J. Phys. Confer. Ser. (2022) 2267, https://doi.org/10.1088/1742-6596/2267/1/012084.
[35] X. Sun, Y. Liu, J. Zhang, L. Hou, J. Sun, C. Yuan, Facile construction of ultrathin SnO_x nanosheets decorated MXene (Ti_3C_2) nanocomposite towards Li-ion batteries as high performance anode materials, Electrochim. Acta. 295 (2019) 237–245, https://doi.org/10.1016/j.electacta.2018.10.152.
[36] M.C. Liu, B.M. Zhang, Y.S. Zhang, D.T. Zhang, C.Y. Tian, L.B. Kong, Y.X. Hu, Interlayer Engineering Construction of 2D Nb_2CT_x with Enlarged Interlayer Spacing Towards High Capacity and Rate Capability for Lithium-Ion Storage, Batteries & Supercaps 4 (2021) 1473–1481, https://doi.org/10.1002/batt.202100083.
[37] A.A. Bolzan, B.J. Kennedy, C.J. Howard, Neutron powder diffraction study of molybdenum and tungsten dioxides, Aust. J. Chem. 48 (1995) 1473–1477, https://doi.org/10.1071/CH9951473.
[38] M. Ghedira, H. Vincent, M. Marezio, J. Marcus, G. Furcaudot, Structure cristalline du conducteur me' tallique bidimensionnel $Mo_4O_{11-\gamma}$, J. Solid State Chem. 56 (1985) 66–73, https://doi.org/10.1016/0022-4596(85)90253-1.
[39] H. Xu, L. Yang, Amorphous MoO_2/C Nanospheres–Porous Graphene Composites for Pseudocapacitive Li Storage, ACS Appl Nano Materials 5 (2022) 13463–13472, https://doi.org/10.1021/acsanm.2c03124.
[40] Y. Wang, D. Kong, W. Shi, B. Liu, G.J. Sim, Q. Ge, H.Y. Yang, Ice Templated Free-Standing Hierarchically WS_2/CNT-rGO Aerogel for High-Performance Rechargeable Lithium and Sodium Ion Batteries, Adv. Energy Mater. 6 (2016), https://doi.org/10.1002/aenm.201601057.
[41] P. Trogadas, V. Ramani, P. Strasser, T.F. Fuller, M.O. Coppens, Hierarchically Structured Nanomaterials for Electrochemical Energy Conversion, Angew. Chem. Int. Ed. 55 (2016) 122–148, https://doi.org/10.1002/anie.201506394.
[42] R.J. Liu, L.X. Yang, Y. Wang, H.P. Bu, H.J. Liu, C.L. Zeng, Characterization and electrochemical properties of submicro-sized orthorhombic V_2C for Li-ion storage, J. Solid State Electrochem. 26 (2022) 831–842, https://doi.org/10.1007/s10008-021-05105-7.
[43] C. Wang, H. Xie, S. Chen, B. Ge, D. Liu, C. Wu, W. Xu, W. Chu, G. Babu, P. M. Ajayan, L. Song, Atomic Cobalt Covalently Engineered Interlayers for Superior Lithium-Ion Storage, Adv Mater 30 (2018) e1802525, https://doi.org/10.1002/adma.201802525.
[44] C. Liu, H. Pan, H. Hu, W. Wei, Q. Lu, C. Zhao, H. Wang, F.J.A.A. Du, Vanadium carbide MXene: as a reductant for the synthesis of gold nanoparticles and its biosensing application, Amino Acids 54 (2022) 1173–1181, https://doi.org/10.1007/s00726-022-03173-1.
[45] Z. Yuan, L. Wang, D. Li, J. Cao, W.J.A.n. Han, Carbon-reinforced Nb_2CT_x MXene/MoS_2 nanosheets as a superior rate and high-capacity anode for sodium-ion batteries, ACS Nano 15 (2021) 7439–7450, https://doi.org/10.1021/acsnano.1c00849.
[46] Y. Sun, X. Hu, W. Luo, Y.H. Huang, Ultrafine MoO_2 nanoparticles embedded in a carbon matrix as a high-capacity and long-life anode for lithium-ion batteries, J. Mater. Chem. 22 (2012) 425–431, https://doi.org/10.1039/C1JM14701C.
[47] X. Han, C.S. Gerke, S. Banerjee, M. Zubair, J. Jiang, N.M. Bedford, E.M. Miller, V.S. J.A.E.L. Thoi, Strategic design of MoO_2 nanoparticles supported by carbon nanowires for enhanced electrocatalytic nitrogen reduction, ACS Energy Lett. 5 (2020) 3237–3243, https://doi.org/10.1021/acsenergylett.0c01857.
[48] J. Tong, Y. Xue, J. Wang, M. Wang, W. Chen, Q. Tian, F.Q. Yu, Cu/Cu_2O nanoparticle–decorated MoO_2 nanoflowers as a highly efficient electrocatalyst for hydrogen evolution reaction, Energy Technol. 8 (2020) 1901392, https://doi.org/10.1002/ente.201901392.
[49] Y. Chu, B. Xi, S.L. Xiong, One-step construction of MoO_2 uniform nanoparticles on graphene with enhanced lithium storage, Chin. Chem. Lett. 32 (2021) 1983–1987, https://doi.org/10.1016/j.cclet.2020.10.024.
[50] Y. Wang, Z. Huang, Y.J. Wang, A new approach to synthesize MoO_2@ C for high-rate lithium ion batteries, J. Mater. Chem A. 3 (2015) 21314–21320, https://doi.org/10.1039/C5TA05345E.
[51] P. Zhang, L. Zou, H. Hu, M. Wang, J. Fang, Y. Lai, J. Li, 3D hierarchical carbon microflowers decorated with MoO_2 nanoparticles for lithium ion batteries, Electrochim. Acta. 250 (2017) 219–227, https://doi.org/10.1016/j.electacta.2017.08.066.
[52] Y. Zhou, Q. Liu, D. Liu, H. Xie, G. Wu, W. Huang, Y. Tian, Q. He, A. Khalil, Y. A. Haleem, T. Xiang, W. Chu, C. Zou, L. Song, Carbon-coated MoO_2 dispersed in three-dimensional graphene aerogel for lithium-ion battery, Electrochimi. Acta. 174 (2015) 8–14, https://doi.org/10.1016/j.electacta.2015.05.153.40578.
[53] G. Zakharova, L. Singer, Z. Fattakhova, S. Wegener, E. Thauer, Q. Zhu, E. Shalaeva, R. Klingeler, Compounds, MoO_2/C composites prepared by tartaric acid and glucose-assisted sol-gel processes as anode materials for lithium-ion batteries, J. Alloys Compd. 863 (2021) 158353, https://doi.org/10.1016/j.jallcom.2020.158353.
[54] S. Petnikota, K.W. Teo, L. Chen, A. Sim, S.K. Marka, M.V. Reddy, V. Srikanth, S. Adams, B.V.R. Chowdari, Exfoliated graphene oxide/MoO_2 composites as anode materials in lithium-ion batteries: an insight into intercalation of Li and conversion mechanism of MoO_2, ACS Appl Mater Interfaces 8 (2016) 10884–10896, https://doi.org/10.1021/acsami.6b02049.
[55] H. Li, A. Li, D. Zhang, Q. Wu, P. Mao, Y. Qiu, Z. Zhao, P. Yu, X. Su, M. Bai, First-Principles Study on the Structural, Electronic, and Lithium Storage Properties of $Ti_3C_2T_2$ (T=O, F, H, OH) MXene, ACS Omega 7 (2022) 40578–40585, https://doi.org/10.1021/acsomega.2c05913.
[56] Y. Xie, M. Naguib, V.N. Mochalin, M.W. Barsoum, Y. Gogotsi, X. Yu, K.-W. Nam, X.-Q. Yang, A.I. Kolesnikov, P.R.S. Kent, Role of surface structure on Li-ion energy storage capacity of two-dimensional transition-metal carbides, J. Am. Chem. Soc. 136 (2014) 6385–6394, https://doi.org/10.1021/ja501520b.
[57] L. Yang, W. Sun, Z. Zhong, J. Liu, Q. Gao, R. Hu, M. Zhu, Hierarchical MoO_2/N-doped carbon heteronanowires with high rate and improved long-term performance for lithium-ion batteries, J. Power Sources. 306 (2016) 78–84, https://doi.org/10.1016/j.jpowsour.2015.11.073.
[58] Z. Wu, S. Zhu, X. Bai, M. Liang, X. Zhang, N. Zhao, C.N. He, One-step in-situ synthesis of Sn-nanoconfined $Ti_3C_2T_x$ MXene composites for Li-ion battery anode, Electrochimi. Acta. 407 (2022) 139916, https://doi.org/10.1016/j.electacta.2022.139916.
[59] G. Mu, D. Mu, B. Wu, C. Ma, J. Bi, L. Zhang, H. Yang, F. Wu, Microsphere-like SiO_2/MXene hybrid material enabling high performance anode for lithium ion batteries, Small 16 (2020) 1905430, https://doi.org/10.1002/smll.201905430.
[60] R.S. Kamat, C. Padwal, H.D. Pham, X. Wang, L.D. Jadhav, D.P. Dubal, Selenium enriched over-oxidized Mo_3Se_4 decorated MXene as a high-performance Li-ion battery anode material, J. Energy Storage. 73 (2023) 108916, https://doi.org/10.1016/j.est.2023.108916.
[61] Y. Jin, S. Tan, Z. Zhu, Y. He, P. Saha, Q. Cheng, Hierarchical MoS_2/C@ MXene composite as an anode for high-performance lithium-ion capacitors, Appl. Surf. Sci. 598 (2022) 153778, https://doi.org/10.1016/j.apsusc.2022.153778.
[62] Z. Zou, Q. Wang, K. Zhu, K. Ye, G. Wang, D. Cao, J. Yan, Ultrathin-walled Bi_2S_3 nanoroll/MXene composite toward high capacity and fast lithium storage, Small 18 (2022) 2106673, https://doi.org/10.1002/smll.202106673.